

# Multiple Visual Features Measurement With Gradient Domain Guided Filtering for Multisensor Image Fusion

Yong Yang, *Senior Member, IEEE*, Yue Que, Shuying Huang, *Member, IEEE*, and Pan Lin, *Member, IEEE*

**Abstract**—Multisensor image fusion technologies, which convey image information from different sensor modalities to a single image, have been a growing interest in recent research. In this paper, we propose a novel multisensor image fusion method based on multiple visual features measurement with gradient domain guided filtering. First, a Gaussian smoothing filter is employed to decompose each source image into two components: approximate component formed by homogeneous regions and detail component with sharp edges. Second, an effective decision map construction model is presented by measuring three key visual features of the input sensor image: contrast saliency, sharpness, and structure saliency. Third, a gradient domain guided filtering-based decision map optimization technique is proposed to make full use of spatial consistency and generate weight maps. Finally, the resultant image is fused with the weight maps and then is experimentally verified through multifocus image, multimodal medical image, and infrared-visible image fusion. The experimental results demonstrate that the proposed method can achieve better performance than state-of-the-art methods in terms of subjective visual effect and objective evaluation.

**Index Terms**—Gradient domain, guided filter, image fusion, multisensor fusion, visual feature measurement.

## I. INTRODUCTION

MULTISENSOR image fusion aims to integrate the complementary information from different sensor images to generate a single fused image. The fused image can provide more comprehensive information about the scene than any of the source images, making it more useful for human and machine perception or further image processing and computer vision tasks [1], [2]. In optical lens imaging, due to the limited depth of the field, the sensors cannot generate images of all

Manuscript received November 1, 2016; accepted December 14, 2016. This work was supported in part by the National Natural Science Foundation of China under Grant 61662026, Grant 61462031, Grant 61262034, and Grant 61473221, in part by the Natural Science Foundation of Jiangxi Province under Grant 20151BAB207033 and Grant 20161ACB21015, and in part by the Project of the Education Department of Jiangxi Province under Grant KJLD14031 and Grant GJJ150461. The Associate Editor coordinating the review process was Dr. Huang-Chen Lee.

Y. Yang and Y. Que are with the School of Information Technology, Jiangxi University of Finance and Economics, Nanchang 330032, China (e-mail: greatyangy@126.com; qki120@163.com).

S. Huang is with the School of Software and Communication Engineering, Jiangxi University of Finance and Economics, Nanchang 330032, China (e-mail: shuyinghuang2010@126.com).

P. Lin is with the Institute of Biomedical Engineering, Xi'an Jiaotong University, Xi'an 710049, China (e-mail: tiger.lin9906@gmail.com).

Color versions of one or more of the figures in this paper are available online at <http://ieeexplore.ieee.org>.

Digital Object Identifier 10.1109/TIM.2017.2658098

objects at various distances with equal clarity [3], which determines the amount of detail an image can convey. This means that a scene cannot simultaneously focus well on all targets only the objects at the focus plane would appear sharp, while others would appear blurred. However, to accurately describe and analyze images, it is desirable to obtain images with every object in focus. An effective solution to this problem uses multifocus image fusion technology, which can create a single ‘all-in-focus’ image in which all of the objects are in focus. The multifocus image fusion has been applied in various applications such as microscopic imaging, remote sensing, and feature extraction [4]. In biomedical imaging, many modalities of medical images are widely used in disease diagnosis, surgery, and radiation therapy. However, the different modalities of medical images convey different information about the human body, organs, and cells, and have their own uses. For example, computed tomography (CT) images can depict dense structures such as bones and hard tissue with less distortion, while magnetic resonance imaging (MRI) images are better visualizations in the case of soft tissues [5]. Similarly, T1-MRI images provide anatomical structure details of tissues, while T2-MRI images provide information about normal and pathological tissues [6]. Using image fusion technologies can obtain more complete descriptions of diseased tissue or organs and increase the effectiveness of image-guided diagnoses. In addition, image fusion techniques are also widely used in infrared and visible image fusion. It has been used to enhance the performance in terms of military, object detection, and target identification [7]. Infrared sensors can capture principally thermal radiations emitted by objects, which are less affected by illumination variation or disguise. Hence, it can overcome some of the obstacles to more clearly detect some objects in low-light, occlusion, and bad weather circumstances. In contrast, visible sensors capture reflected lights with abundant detail information, and also provide more natural intensities and contrasts for human visual perception [8].

Within the past two decades, a great variety of multisensor image fusion algorithms have been proposed in the literature. Among these methods, multiscale transform-based methods are the most popular algorithms used in various image fusion scenarios because they can preserve the details of different source images and are simple to implement [9]. Specifically, these methods include pyramid-based methods such as Laplacian pyramid (LP) [10] and gradient pyramid [11] and wavelet-based methods such as discrete wavelet

transform (DWT) [12], shift-invariant DWT (SIDWT) [13], and dual-tree complex wavelet transform [14]. Recently developed multiscale geometric analysis tools are very successful methods with higher directional sensitivity than wavelets. For example, curvelet transform [15], shearlet transform [16], and contourlet transform [17]. In particular, as the shift-invariant version of contourlet transform, nonsubsampled contourlet transform (NSCT) can solve the pseudo-Gibbs phenomena around singularities and provide an asymptotic optimal representation of images compared with other transform tools [18]. It has been successfully applied to image fusion and can generally achieve the best performance [6], [19]. However, the practical applications of the NSCT are limited because it is time consuming and its implementation is complex.

Pulse coupled neural networks (PCNNs) have also been successfully employed in many image processing applications including image fusion [20], [21]. It was proposed in [22] to simulate the processing mechanism of a cat's visual cortex. Based on the PCNN bionic mechanism and pulse synchronization of neuron characteristics, PCNN plays an important role in image fusion. However, the PCNN is very complex and has a large number of free parameters [23]. In addition, the optimal parameters that set PCNN for different images have poor versatility and the fusion performance is often sensitive to them. Das and Kundu [24] used an adaptive reduced PCNN (RPCNN) for medical image fusion. RPCNN has a less complex structure and fewer parameters. However, besides method [24], it is usually that the PCNN used in multiscale transform domain can be a better result. Thus, the problem of inefficiency still remains.

In the past few years, the applications of compressive sensing [25] and sparse representation (SR) [3], [4], [26] in computer vision have become a popular topic in current research. Despite the advantage of reducing the computational complexity and simultaneously enhancing the quality of the fused image, there are two main limitations in image fusion. First, the randomness of measurement matrix may result in a lack of spatial information in compressed measurements and high reconstruction error [27]. In addition, it is well known that an over-complete dictionary is at the core of the sparsity model and determines the performance of image fusion methods [28]. However, the over-complete dictionary learning is time consuming and the atom selection in dictionary construction is a difficult problem. Liu *et al.* [29] present a general image fusion framework by combining multiscale transform and SR. It can achieve better results when compared with traditional multiscale transform-based and SR-based methods.

The above approaches have a common drawback that may produce brightness because spatial consistency is not well considered in the fusion process [37]. To make full use of spatial context, simple and efficient spatial domain-based methods have been widely researched in recent years [30]–[32]. In spatial domain methods, fusion rules are directly applied to image pixels or image regions according to some image feature measure. The main defects of these methods are misalignment of the decision map with the boundary of objects and wrong decisions in subregions of the salient or flat regions that produce undesirable artifacts in the final fused image [33].

To overcome this problem, some spatial techniques and optimization approaches are used for image fusion such as cross bilateral filter (CBF) [34], generalized random walks [35], and Markov random fields [36]. These methods use the weighted average of pixel values for fusing the source images by estimating spatially smooth and edge-aligned weights. However, these weight construction and global optimization methods may lead to contrast decrease, inefficiency, and over-smooth the resulting weights. To solve these problems, Li *et al.* [37] presented a guided filtering-based method (GFF) that can obtain better results with high computational efficiency. However, the weight map construction method by the Laplace operator to generate pixel saliency does not do a good job representing visually discernable features in source images. Moreover, another drawback is the possibility of halos because the local linear model used in the guided image filter (GIF) cannot represent the image well near some edges.

Based on the above analysis, the main contributions of this paper over current methods can be summarized as follows.

- 1) This paper proposes a novel multisensor image fusion scheme based on multiple visual features measurement and gradient domain guided filtering. The process of fusion consists of three stages: constructing initial decision map, optimizing initial decision map, and fusing source images.
- 2) In the process of constructing initial decision map, we present a model for image fusion by incorporating contrast saliency, sharpness, and structural saliency as the key visual factors. The model can effectively measure the significance of visual features, which greatly improves the performance of the proposed method.
- 3) Instead of using traditional optimization-based and guided filtering-based methods, gradient domain guided filtering is proposed to optimize the initial decision maps by considering the correlations between neighborhood pixels. The halo artifacts can be more effectively suppressed in this way. In addition, the gradient domain GIF (GDGIF) is less sensitive to parameter selection and has the same complexity as the GIF.
- 4) Furthermore, the proposed method can provide a better performance than a series of state-of-the-art fusion approaches for different types of source images including multifocus images, multimodal medical images, and infrared-visible images.

The rest of this paper is organized as follows. The gradient domain guided image filtering theory is briefly introduced in Section II. The proposed image fusion method is described in Section III. The experimental results and analysis are depicted in Section IV, and the conclusions are given in Section V.

## II. GRADIENT DOMAIN GUIDED IMAGE FILTERING

GIF [38] is a well-known local linear translation-variant filter for its edge-preserving property with low computational complexity. The filtering output is locally a linear transform of the guidance image, and it can make the filtering output more structured and less smoothed than the input. This makes it possible to transfer structure from the guidance image to the

output, even if the filtering input is smooth. It is an important property to achieve the binary map refining near the object boundaries for image fusion. GIF has lots of applications in image processing and computer vision, such as image detail enhancement, joint upsampling, and image fusion [37], [38]. However, the model cannot represent the image well near some of the edges [39]. As a result, there may be some halos in the images. Li *et al.* [39] propose a weighted GIF to reduce the halo artifacts of the GIF by introducing an edge aware factor. Nevertheless, they cannot preserve edges well in some cases because there are no explicit constraints to treat edges and consider the image filtering with edge-preserving processes together [40].

In [40], a GDGIF was proposed by incorporating an explicit first-order edge-aware constraint. It can represent the images more accurately near edges, and the performance of preserved edges is highly improved. Hence, it preserves edges better than the GIF.

#### A. Edge-Aware Weighting

Let  $I$  be a guidance image,  $\sigma_{I,1}(k)$  be the variance of  $I$  in the  $3 \times 3$  window, and  $\sigma_{I,r_1}(k)$  be the variance of  $I$  in the  $(2r_1+1) \times (2r_1+1)$  window. An edge-aware weighting  $\Gamma_I(k)$  is defined by

$$\Gamma_I(k) = \frac{1}{M} \sum_{i=1}^M \frac{\chi(k) + \varepsilon}{\chi(i) + \varepsilon} \quad (1)$$

where  $\chi(k)$  is defined as  $\sigma_{I,1}(k)\sigma_{I,r_1}(k)$  and  $r_1$  is the window size of the filter.  $M$  denotes the total number of pixels in an image. The weighting  $\Gamma_I(k)$  measures the importance of pixel  $k$  with respect to the whole guidance image. With this weighting, the edges are detected more accurately.

#### B. Gradient Domain Guided Filter

As with the GIF, the key assumption of the GDGIF is a local linear model between the guidance image  $I$  and the filtering output  $Z$ . The model ensures that the output  $Z$  has an edge only if the guidance image  $I$  has an edge

$$Z(i) = a_k I(i) + b_k, \quad \forall i \in \omega_k \quad (2)$$

where  $\omega_k$  is a square window of size  $(2r+1) \times (2r+1)$ , and  $a_k$  and  $b_k$  are two constants in the  $\omega_k$  window. The two constants can be obtained by minimizing the difference between the images to be filtered  $X$  and the filtering output  $Z$

$$E = \sum_{i \in \omega_k} \left[ (a_k I(i) + b_k - X(i))^2 + \frac{\lambda}{\Gamma_I(k)} (a_k - \gamma_k)^2 \right] \quad (3)$$

where  $\lambda$  is a regularization parameter as with the GIF and  $\gamma_k$  is defined as

$$\gamma_k = 1 - \frac{1}{1 + e^{\eta(\chi(k) - \mu_{\chi,\infty})}} \quad (4)$$

where  $\mu_{\chi,\infty}$  is the mean value of all  $\chi(i)$ , and  $\eta$  is calculated as  $4/(\mu_{\chi,\infty} - \min(\chi(i)))$ . It is worth noting that the value of  $\gamma_k$  approaches 1 if the pixel  $k$  is at an edge and 0 if it is in a smooth region. Hence, this filter is less sensitive to the selection of  $\lambda$  that is set to  $10^{-5}$  in this paper.

The optimal values of  $a_k$  and  $b_k$  are computed as

$$a_k = \frac{\mu_{I \odot X, r_1}(k) - \mu_{I, r_1}(k)\mu_{X, r_1}(k) + \frac{\lambda}{\Gamma_I(k)}\gamma_k}{\sigma_{I, r_1}^2(k) + \frac{\lambda}{\Gamma_I(k)}} \quad (5)$$

$$b_k = \mu_{X, r_1}(k) - a_k \mu_{I, r_1}(k). \quad (6)$$

The final value of  $Z(i)$  is given as follows:

$$Z(i) = \bar{a}_i I(i) + \bar{b}_i \quad (7)$$

where  $\bar{a}_i$  and  $\bar{b}_i$  are the mean values of  $a_k$  and  $b_k$  in the window, respectively, computed as

$$\bar{a}_i = \frac{1}{|\omega|} \sum_{k \in \omega} a_k, \quad \bar{b}_i = \frac{1}{|\omega|} \sum_{k \in \omega} b_k \quad (8)$$

and  $|\omega|$  is the number of pixels in  $\omega_k$ . For further information on GDGIF, see [40].

For simplicity, we rewrite gradient domain guided filtering operation as  $GF_r(X, I)$  in this paper. Herein, the radius of the window is  $r$ . Moreover,  $X$  and  $I$  refer to the input image and guidance image, respectively.

### III. PROPOSED METHOD

This section provides a more detailed description of the proposed fusion method. First of all, a Gaussian filtered result of each source image is perceived as its approximate component, and the detail component can be easily obtained by subtracting the approximate component from the  $n$  th source image  $I_n$  as follows:

$$I_n^A = I_n * G_{r,\sigma} \quad (9)$$

$$I_n^D = I_n - I_n^A \quad (10)$$

where  $I_n^A$  and  $I_n^D$  are the approximate and detail component of the  $n$  th source image, respectively,  $*$  denotes a convolution operator, and  $G_{r,\sigma}$  is a Gaussian smoothing filter with size  $(2r+1)(2r+1)$  and standard deviation  $\sigma$ . The parameters  $r$  and  $\sigma$  are set to 20 and 5, respectively.

This step can separate each source image into an approximate component containing the main variations in intensity and a detail component containing the abundant detail information.

#### A. Multiple Visual Feature Measurement for Decision Map

According to [41], contrast preservation, sharpness, and structure preservation are three critically important characteristics in accounting for the visual quality of a fused image given source images. It is thus desirable to design our method to separate the decision map into the measurement of three key visual features of input images: contrast saliency, sharpness, and structure saliency.

**1) Contrast Saliency Measure:** The human visual system (HVS) is not sensitive to a single pixel, but is sensitive to changes in the local neighborhoods of pixels. Hence, we use the local contrast to construct decision map to make full use of the corresponding image's local features. Using the standard deviation can lead to a simple, useful, and robust local contrast measure [42]. We measure contrast locally using a sliding window approach, which results in a map that indicates the

spatial variation of local contrast. The local contrast is defined by the following equation:

$$LC = \left( \frac{1}{O \times P} \sum_{o=1}^O \sum_{p=1}^P (I(x+o, y+p) - \hat{\mu}(x, y))^2 \right)^{1/2} \quad (11)$$

where  $\hat{\mu}$  denotes the mean value of the window centered on the spatial location  $(x, y)$  and  $(O \times P)$  is the window size. Then, the local average of the value of local contrast is used to construct the contrast saliency (CS) maps

$$CS = LC * G_{r,\sigma} \quad (12)$$

where  $G_{r,\sigma}$  is a Gaussian filter. The measured contrast saliency maps provide good characterization of the saliency level of detail information. The input image's pixel that has the higher contrast saliency is the more informative. Next, the contrast saliency maps are compared to generate the decision map  $D_{1,n}^k$  as follows:

$$D_{1,n}^k = \begin{cases} 1, & \text{if } CS_n^k = \max(CS_1^k, CS_2^k, \dots, CS_N^k) \\ 0 & \text{otherwise} \end{cases} \quad (13)$$

where  $N$  is the number of source images and  $CS_n^k$  is the contrast saliency value of the pixel  $k$  in the  $n$  th image.

2) *Sharpness Measure*: Sharpness is an important feature in visual perception of images. Several sharpness measures have been devised and applied to image fusion such as energy of image gradient, variance of image intensities, energy of Laplacian of the image, sum-modified Laplacian (SML), and spatial frequency [43]. According to objective assessments in [43], SML is the preferred sharpness measure in spatial domain. In the case of the Laplacian, the second derivatives in the  $x$  and  $y$  directions can have opposite signs and tend to cancel each other [44]. Therefore, the expression for the discrete approximation of modified Laplacian (ML) is

$$\nabla_{ML}^2 I(x, y) = |2I(x, y) - I(x - \text{step}, y) - I(x + \text{step}, y)| + |2I(x, y) - I(x, y - \text{step}) - I(x, y + \text{step})|. \quad (14)$$

Using a variable spacing (*step*) between the pixels to compute ML can accommodate for possible variations in the size of texture elements. In this paper, *step* always equals 1. The definition of sharpness map is defined as follows:

$$SP(x, y) = \sum_{m=-M_1}^{M_1} \sum_{n=-N_1}^{N_1} [\nabla_{ML}^2 I(x+m, y+n)] \quad (15)$$

for a window with size  $(2M_1+1)(2N_1+1)$ . The sharpness map can reflect the marginalized mutation and clarity information of an image. The sharpness maps are compared to generate the decision map  $D_{2,n}^k$  as follows:

$$D_{2,n}^k = \begin{cases} 1, & \text{if } S_n^k = \max(S_1^k, S_2^k, \dots, S_N^k) \\ 0, & \text{otherwise} \end{cases} \quad (16)$$

where  $N$  is the number of source images and  $S_n^k$  is the sharpness value of the pixel  $k$  in the  $n$  th image.

3) *Structure Saliency Measure*: As is well known, HVS is highly adapted to extracting structural information from a scene. Here, we introduce the structural saliency model [45] to construct decision map that truly reflects the saliency of the local image structure and the discriminative response of HVS to the different image structural stimuli, since local image structure is closely related to the local gradient covariance. Consider a single-valued image  $I(x, y)$  for which the gradient covariance matrix over a local window  $W$  is defined as

$$C = \begin{pmatrix} \sum_{X \in W} I_x^2(X) & \sum_{X \in W} I_x(X)I_y(X) \\ \sum_{X \in W} I_x(X)I_y(X) & \sum_{X \in W} I_y^2(X) \end{pmatrix} \quad (17)$$

where  $I_x(X)$  and  $I_y(X)$  denote the gradients along the  $x$  and  $y$  directions at a given position  $X = (x, y)$ . To obtain the representation of local image structure, we decompose  $C$  through eigenvalue decomposition as follows:

$$C = V \begin{pmatrix} s_1^2 & \\ & s_2^2 \end{pmatrix} V^T. \quad (18)$$

The local image structure is then related to the eigenvalues of this matrix. This saliency measure approach to local image structure is able to give a steady description of image structure that is robust to both blurring and random noise. Meanwhile, it works for all of the types of structures including ridge, edge, and corner. Therefore, the image structure saliency (SS) map can be defined as

$$SS = \sqrt{(s_1 + s_2)^2 + \alpha(s_1 - s_2)^2} \quad (19)$$

where  $\alpha > -1$ . This parameter is mainly used to determine the relative emphasis that the structure saliency puts on the corner-like structures. The structure saliency maps are compared to generate the decision map  $D_{3,n}^k$  as follows:

$$D_{3,n}^k = \begin{cases} 1 & \text{if } SS_n^k = \max(SS_1^k, SS_2^k, \dots, SS_N^k) \\ 0 & \text{otherwise} \end{cases} \quad (20)$$

where  $N$  is the number of source images and  $SS_n^k$  is the structure saliency value of the pixel  $k$  in the  $n$  th image.

### B. Gradient Domain Guided Filtering for Weight Map

The decision maps obtained above are usually noisy and not aligned with object boundaries (see Fig. 1), which may produce artifacts in the fused image because the spatial consistency is not considered. Spatial consistency means that if two adjacent pixels have similar brightness, they will tend to have similar weights. Using existing global smoothing filters to obtain the desired weight maps can avoid halo artifacts. However, these global optimization-based algorithms are used to formulate an energy function and find the global optimal solution after a number of iterations, so they are usually inefficient [37]. As the GIF complies with the principle of spatial consistency and low computational complexity, applying the guided filtering for initial decision maps can generate the optimized weighting maps. Nevertheless, the local linear model used in GIF cannot represent the image well near some edges. The GDGIF proposed an edge-aware constraint

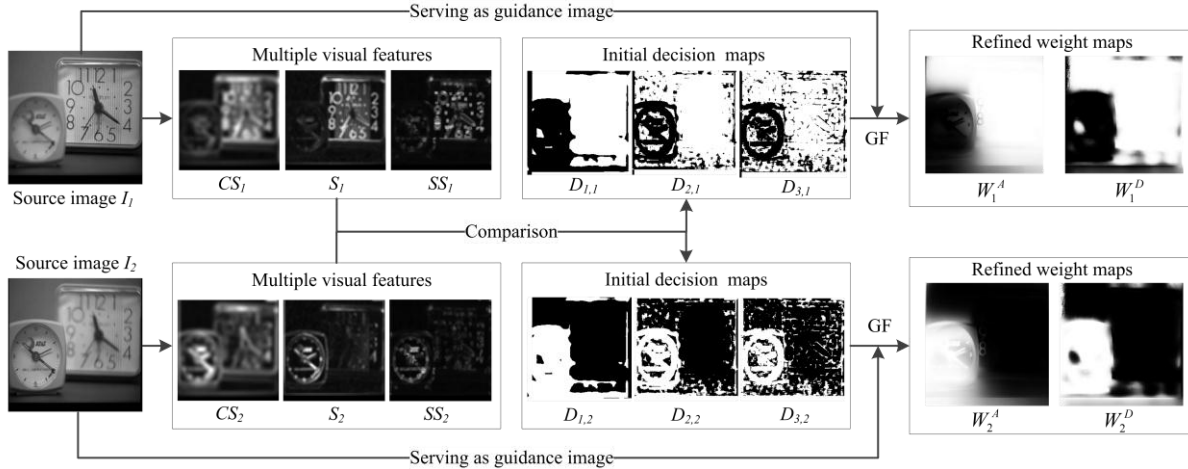


Fig. 1. Schematic of the weight map construction model.

by incorporating an explicit first order and makes edges be preserved better. In addition, as the GDGIF is less sensitive to the blur degree parameter selection, it can enhance the versatility for practical applications.

Hence, we propose to apply the gradient domain guided filtering to each visual feature-based decision map \$D\_{1,n}\$, \$D\_{2,n}\$, and \$D\_{3,n}\$ with the corresponding source image \$I\_n\$ serving as the guidance image to generate the ultimate weight maps

$$W_{m,n}^A = GF_{r1}(D_{m,n}, I_n) \quad (21)$$

$$W_{m,n}^D = GF_{r2}(D_{m,n}, I_n) \quad (22)$$

where \$r\_1\$ and \$r\_2\$ are the parameters of the GDGIF and \$m = (1, 2, 3)\$.

The weight maps based on contrast saliency, sharpness, and structure saliency measures described above address different aspects about visual features of the source images and are complementary to one another. By combining these calculations, we obtain overall weight maps with the corresponding source image \$I\_n\$ given by

$$W_n^A = \prod_{m=1}^3 W_{m,n}^A \quad (23)$$

$$W_n^D = \prod_{m=1}^3 W_{m,n}^D \quad (24)$$

where \$W\_n^A\$ and \$W\_n^D\$ are the resulting weight maps of the low- and high-frequency components. Finally, the values of the \$N\$ weight maps are normalized such that they sum to one at each pixel \$k\$. Fig. 1 summarizes the main processes of weight map construction.

### C. Fuse Images

The approximate and detail components of different source images are fused together by weighted averaging

$$I_F^A = \sum_{n=1}^N W_n^A I_n^A \quad (25)$$

$$I_F^D = \sum_{n=1}^N W_n^D I_n^D. \quad (26)$$

Finally, the fused image \$F\$ can be synthesized with the fused approximate and detail components

$$F = I_F^A + I_F^D. \quad (27)$$

## IV. EXPERIMENTS AND DISCUSSION

In this section, we will perform experiments to verify the feasibility of our proposed image fusion method for multifocus image, multimodal medical image, and infrared-visible image over the standard test images. Among them, there are five pairs of each type of image and the two source images are perfectly preregistered for each pair (see Fig. 2). Since image registration is out of the scope of this paper, a thorough survey of image registration techniques can be referred to [46]. The proposed fusion method is compared with seven state-of-the-art image fusion algorithms that are based on LP [10], DWT [12], NSCT [18], NSCT-PCNN [20], NSCT-SR [29], CBF [34], and GFF [37]. Three decomposition levels, the ‘‘averaging’’ scheme for the low-pass sub-band, and the absolute maximum choosing scheme for the bandpass sub-band are adopted for the LP, DWT, and NSCT methods. In addition, the default parameters given by the respective authors are adopted for the NSCT-SR-, NSCT-PCNN-, CBF-, and GFF-based methods.

In this paper, the GDGIF sizes \$r\_1\$ and \$r\_2\$ are two main parameters that may affect the final fusion result. The weight maps should generally be consistent with their corresponding components. In other words, spatially smooth weights are preferred for fusing the approximate components to prevent artificial edges producing. By contrast, the detail components are sharp, and thus the corresponding weights should also be sharp. Otherwise, details may be lost if the corresponding weights are over-smoothed. On the other hand, a default value of \$r\$ is set to 16 and it has different settings in a variety of applications [38]–[40]. Therefore, through the trial and error, the large filter size \$r\_1\$ is set to 40 for fusing the approximate components, while the small filter size \$r\_2\$ is set to 10 for fusing the detail components.

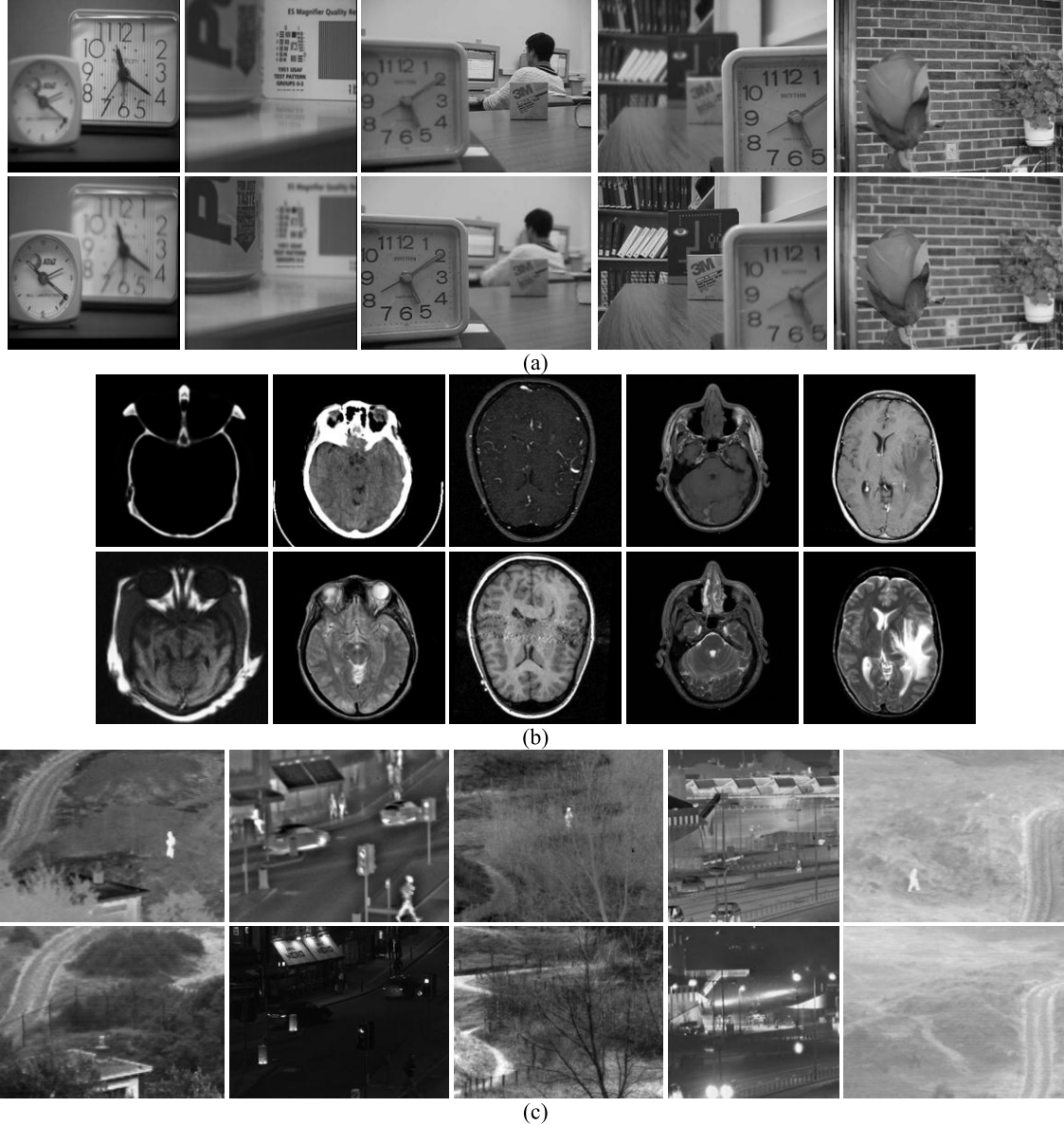


Fig. 2. Samples of source image pairs used in experiments. (a) Multifocus image pairs. (b) Multimodal medical image pairs. (c) Infrared and visible image pairs.

#### A. Objective Quality Evaluation Metrics

It is well known that different image quality metrics measure the visual quality of images from different aspects, but none of them can directly measure the quality. In this paper, to assess the fusion performance of different methods objectively, we consider both the visual representation and the quantitative assessment of the fused images. We have considered three popular fusion performance metrics as defined in the following. The default parameters given in the related publications are adopted for these quality indexes.

*1) Mutual Information:* Mutual information (*MI*) [47] can indicate how much information the fused image conveys about the source images. *MI* between the fusion image and the source image is defined as follows:

$$MI = MI^{AF} + MI^{BF} \quad (28)$$

in which

$$MI^{AF} = \sum_{f=0}^L \sum_{a=0}^L p^{AF}(a, f) \log_2 \left( \frac{p^{AF}(a, f)}{p^A(a)p^F(f)} \right) \quad (29)$$

$$MI^{BF} = \sum_{f=0}^L \sum_{b=0}^L p^{BF}(b, f) \log_2 \left( \frac{p^{BF}(b, f)}{p^B(b)p^F(f)} \right) \quad (30)$$

where  $MI^{AF}$  and  $MI^{BF}$  denote the normalized MI between the fused image and the source images A and B;  $a$ ,  $b$ , and  $f \in [0, L]$ .  $p^A(a)$ ,  $p^B(b)$ , and  $p^F(f)$  are the normalized gray level histograms of the source images and the fused image.  $p^{AF}(a, f)$  and  $p^{BF}(b, f)$  are the joint gray level histograms between the fused image and the source images A and B. The greater the value of *MI* is, the better the fusion effect will be.

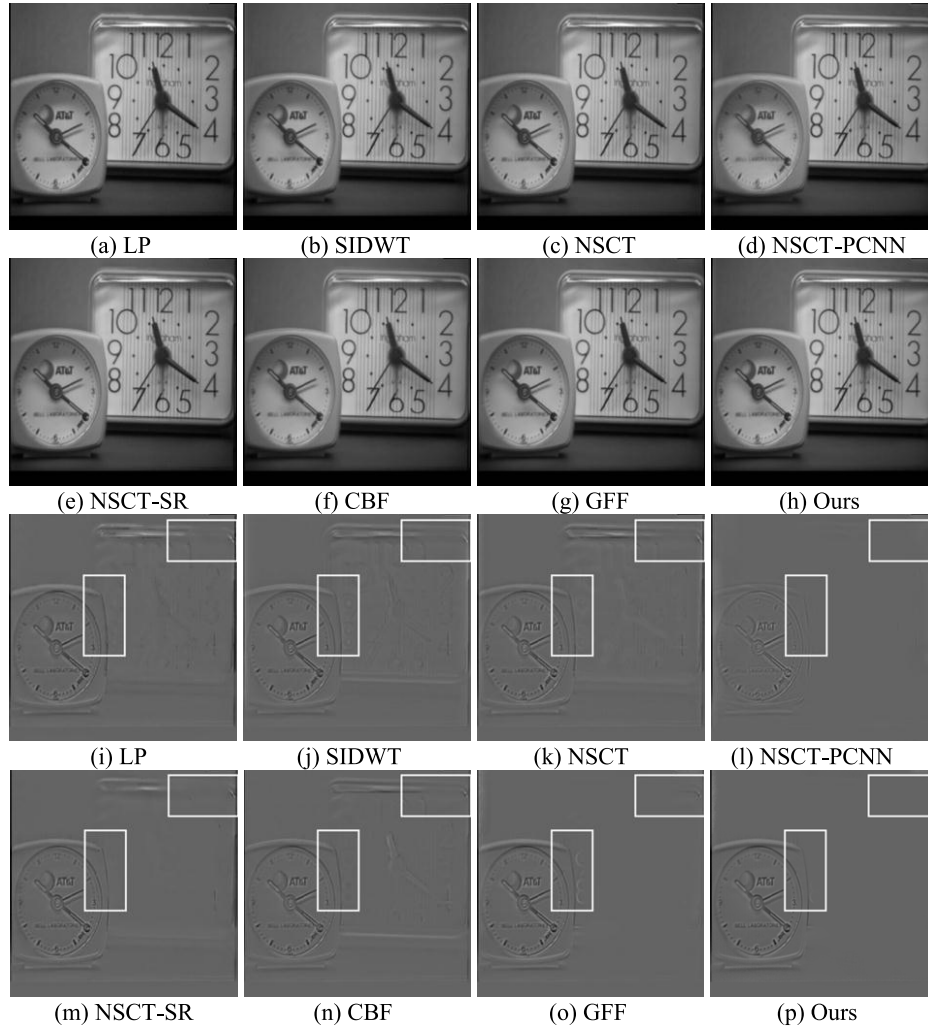


Fig. 3. Experimental results of fusing the multifocus image ‘clock.’ (a)–(h) Fusion results of different fusion algorithms. (i)–(p) Difference images between fused images and source image of right focused.

2) *Gradient-Based Fusion Metric*: The gradient based index ( $Q^{AB/F}$ ) proposed in [48] measures the similarity between the edges transferred from the source images to the fused image. The definition is given as

$$Q^{AB/F} = \frac{\sum_{i=1}^M \sum_{j=1}^N [Q^{AF}(i, j)w^A(i, j) + Q^{BF}(i, j)w^B(i, j)]}{\sum_{i=1}^M \sum_{j=1}^N [w^A(i, j) + w^B(i, j)]} \quad (31)$$

in which

$$Q^{AF}(i, j) = Q_a^{AF}(i, j)Q_g^{AF}(i, j) \quad (32)$$

$$Q^{BF}(i, j) = Q_a^{BF}(i, j)Q_g^{BF}(i, j) \quad (33)$$

where  $w^A(i, j)$  and  $w^B(i, j)$  are the corresponding gradient strengths for images A and B, respectively.  $M$  and  $N$  are the width and height of the images, while  $Q_a^{XF}(i, j)$  and  $Q_g^{XF}(i, j)$  are the edge strength and orientation preservation values at location  $(i, j)$  for each source image. The  $Q^{AB/F}$  is a popular fusion metric that computes the amount of gradient

information injected into the fused image from the source images.

3) *Structural Similarity-Based Fusion Metric*: Yang *et al.*’s [49] metric  $Q_Y$  uses structural similarity (SSIM) for fusion quality assessment and is defined as follows:

$$Q_Y = \begin{cases} \tau(w)\text{SSIM}(A, F|w) + (1 - \tau(w))\text{SSIM}(B, F|w), & \text{for } \text{SSIM}(A, B|w) \geq 0.75 \\ \max\{\text{SSIM}(A, F|w), \text{SSIM}(B, F|w)\}, & \text{for } \text{SSIM}(A, B|w) < 0.75 \end{cases} \quad (34)$$

where  $w$  is a window of size  $7 \times 7$ ,  $A$  and  $B$  are the source images, and  $F$  is the fused image. SSIM is the structural similarity [42], and the local weight  $\tau(w)$  is calculated as follows:

$$\tau(w) = \frac{s(A|w)}{s(A|w) + s(B|w)} \quad (35)$$

where  $s(A|w)$  and  $s(B|w)$  are the variance of source images  $A$  and  $B$  within the window  $w$ , respectively.  $Q_Y$  measures how well the structural information of source images is preserved.

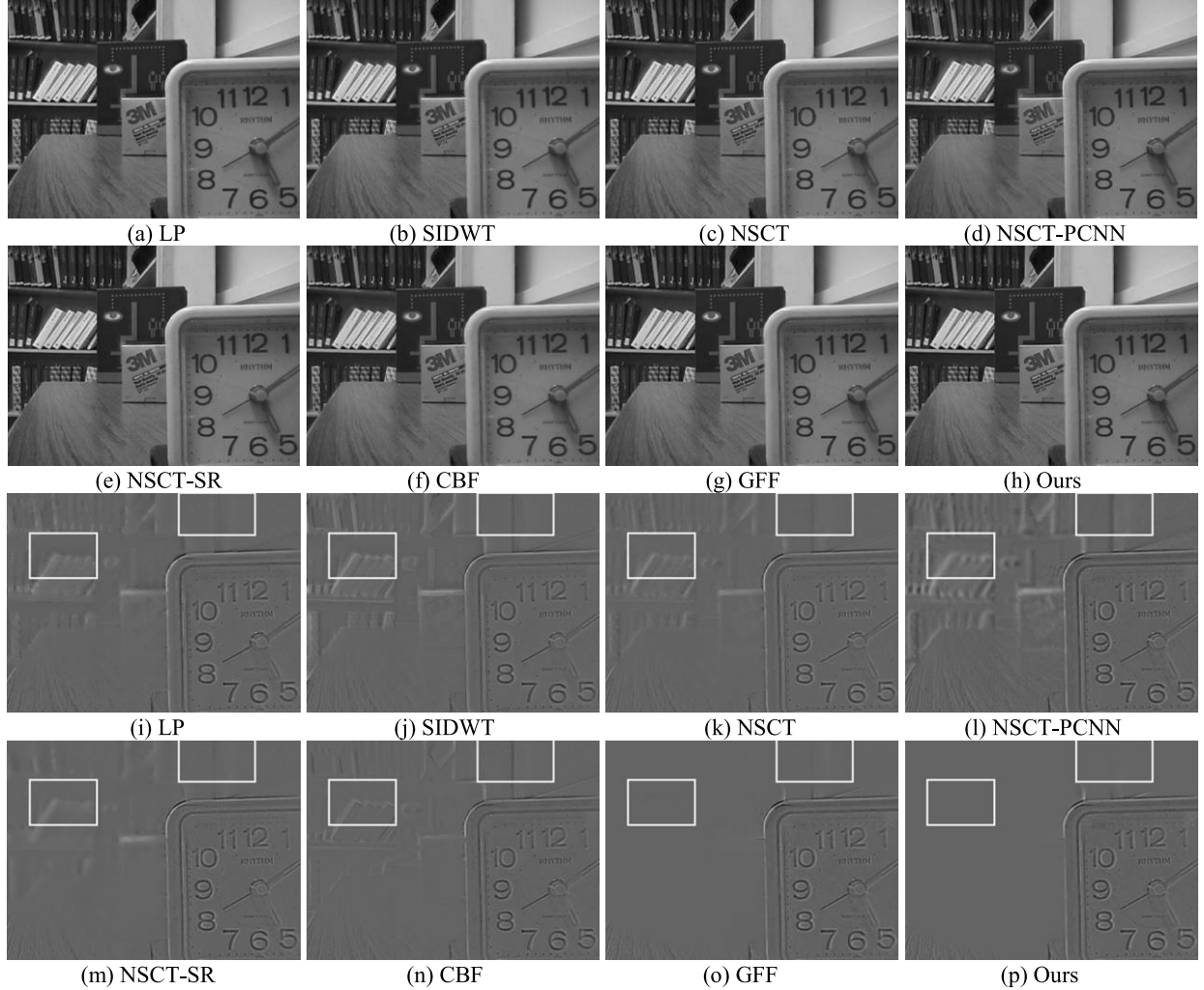


Fig. 4. Experimental results of fusing the multifocus image ‘disk.’ (a)–(h) Fusion results of different fusion algorithms. (i)–(p) Difference images between fused images and source image of left focused.

TABLE I  
EVALUATION INDICES FOR FUSED MULTIFOCUS IMAGES

Inputs	Index	LP	SIDWT	NSCT	NSCT-PCNN	NSCT-SR	CBF	GFF	Ours
clock	$MI$	7.0870	6.8513	7.0022	7.5962	7.4622	7.6895	8.0167	<b>8.3548</b>
	$Q^{AB/F}$	0.7030	0.7156	0.7100	0.7174	0.7245	0.7426	0.7448	<b>0.7500</b>
	$Q_Y$	0.9054	0.9075	0.9168	0.9245	0.9279	0.9447	0.9601	<b>0.9655</b>
pepsi	$MI$	7.2502	7.0450	7.3637	7.8419	7.5737	7.8554	8.3025	<b>8.7410</b>
	$Q^{AB/F}$	0.7172	0.7166	0.7209	0.7325	0.7282	0.7453	0.7531	<b>0.7585</b>
	$Q_Y$	0.9140	0.9175	0.9228	0.9297	0.9326	0.9311	0.9554	<b>0.9672</b>
lab	$MI$	7.2556	7.1326	7.3461	7.6369	7.5188	7.6774	8.1984	<b>8.6465</b>
	$Q^{AB/F}$	0.7220	0.7276	0.7292	0.7125	0.7443	0.7535	0.7588	<b>0.7612</b>
	$Q_Y$	0.9251	0.9323	0.9390	0.9088	0.9236	0.8983	0.9566	<b>0.9637</b>
disk	$MI$	6.2668	6.0652	6.2624	6.3114	6.5611	6.7750	7.5524	<b>8.0461</b>
	$Q^{AB/F}$	0.6728	0.6879	0.6812	0.6558	0.7028	0.7059	0.7211	<b>0.7253</b>
	$Q_Y$	0.9257	0.9302	0.9384	0.9077	0.9536	0.9410	0.9758	<b>0.9851</b>
flower	$MI$	5.5324	5.0508	5.5306	5.0080	5.7426	5.8729	7.0911	<b>7.8296</b>
	$Q^{AB/F}$	0.7510	0.7572	0.7672	0.7432	0.7643	<b>0.7864</b>	0.7822	0.7805
	$Q_Y$	0.9443	0.9413	0.9538	0.9359	0.9554	0.9603	<b>0.9605</b>	0.9601

### B. Experiments on Multifocus Image Fusion

The first experiment was performed on five pairs of multifocus images, including *clock*, *pepsi*, *lab*, *disk*, and *flower*

[see Fig. 2(a)], which are used to demonstrate the validity of the proposed method. Two examples from fusion results and the difference images of multifocus data set are shown

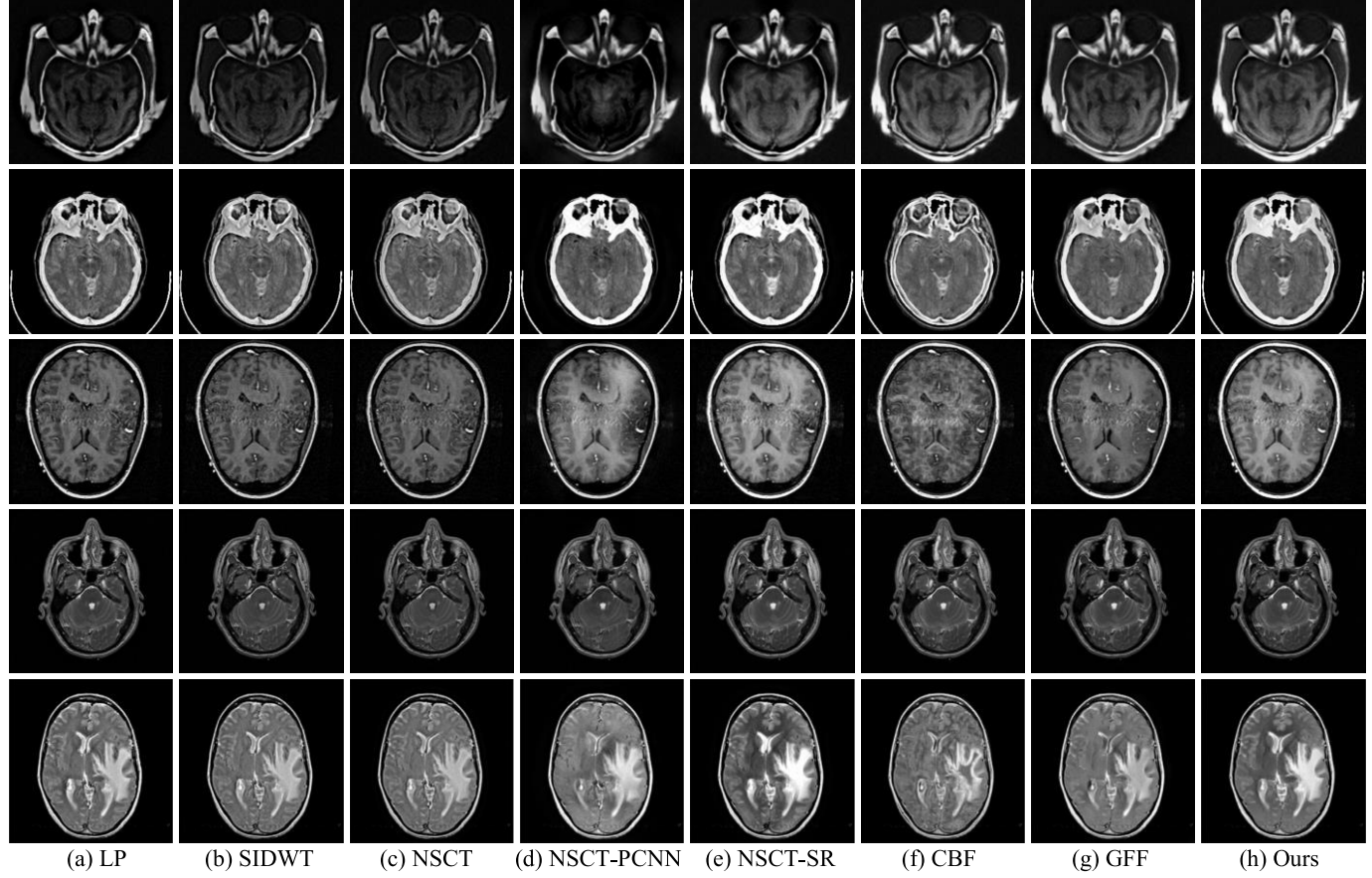


Fig. 5. Experimental results of fusing the five pairs of multimodal medical images. (a)–(h) Fusion results of different fusion algorithms.

TABLE II  
EVALUATION INDICES FOR FUSED MULTIMODAL MEDICAL IMAGES

Inputs	Index	LP	SIDWT	NSCT	NSCT-PCNN	NSCT-SR	CBF	GFF	Ours
group 1 CT/MRI	$MI$	2.5566	2.6935	2.5573	1.3062	3.0503	4.8909	3.2685	<b>5.2506</b>
	$Q^{AB/F}$	0.7309	0.7221	0.6913	0.6289	0.7458	0.7911	0.7858	<b>0.8086</b>
	$Q_Y$	0.6736	0.7004	0.7002	0.5320	0.8523	0.9260	0.8825	<b>0.9554</b>
group 2 CT/MRI	$MI$	2.4837	2.4879	2.4393	2.6800	2.6351	2.8108	2.7461	<b>2.8962</b>
	$Q^{AB/F}$	0.6082	0.6183	0.5994	0.5601	0.6187	<b>0.6459</b>	0.6259	0.6383
	$Q_Y$	0.8730	0.8717	0.7088	0.6053	0.7276	0.8925	0.8811	<b>0.9378</b>
group 3 MR-T1/MRA	$MI$	3.3521	3.4920	3.4469	3.0354	4.4684	3.7450	3.5999	<b>4.7197</b>
	$Q^{AB/F}$	0.5872	0.5985	0.5926	0.5272	0.6426	0.5664	0.6230	<b>0.6741</b>
	$Q_Y$	0.7587	0.8066	0.8087	0.7315	0.8867	0.7765	0.8268	<b>0.9364</b>
group 4 MR-T1/MR-T2	$MI$	3.5281	3.4471	3.4207	3.5733	3.6744	4.1219	4.1640	<b>4.5717</b>
	$Q^{AB/F}$	0.6855	0.6982	0.6862	0.6581	0.7154	0.7150	<b>0.7384</b>	0.7359
	$Q_Y$	0.7908	0.8386	0.8271	0.8345	0.8574	0.8639	0.9519	<b>0.9729</b>
group 5 MR-GAD/MR-T2	$MI$	3.3592	3.3400	3.2716	3.3846	3.6336	3.5502	3.4190	<b>3.6121</b>
	$Q^{AB/F}$	0.5876	0.5966	0.5848	0.5707	0.6419	0.5991	0.6288	<b>0.6565</b>
	$Q_Y$	0.8872	0.8657	0.7442	0.7107	0.7876	0.8530	0.8678	<b>0.9287</b>

in Figs. 3 and 4 for visual comparison. The difference images between fused images and the input images allow for better comparison of the effect of fused images. For the focused areas, the difference between the fused image and the input image should be less. In contrast, for the unfocused areas, the difference image should be clear and have more details.

It can be seen that the fusion results of the fusion methods seem to perform well for multifocus images. However, careful comparison of the difference images indicates that the proposed method is superior to other fusion methods. As shown in the rectangular region of Fig. 3(i)–(o), different degrees of residual errors exist in the difference images of other seven methods. Obviously, we can observe similar

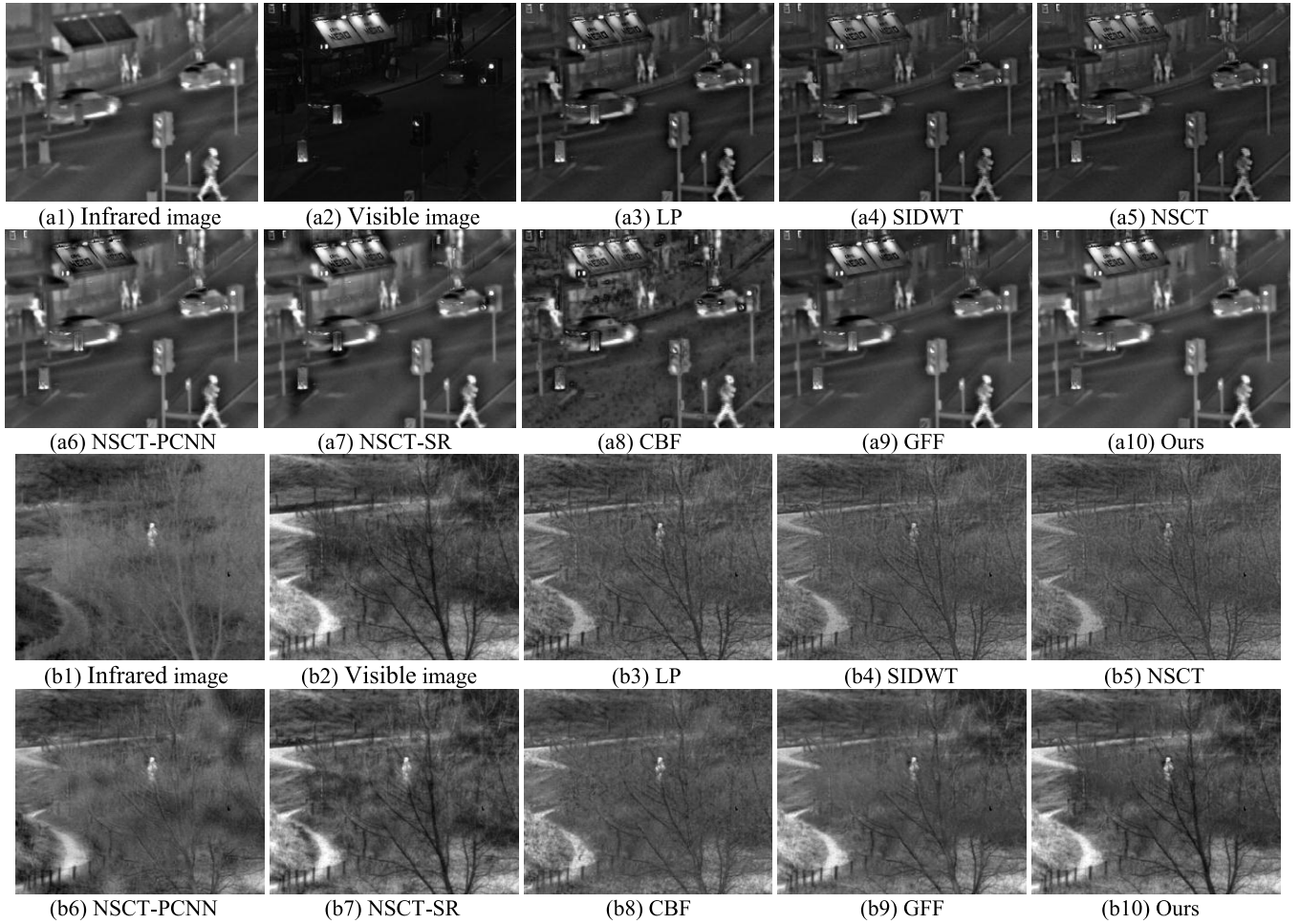


Fig. 6. Two experimental result examples of fusing the infrared and visible image. (a1)–(a10) First fusion results of different fusion algorithms. (b1)–(b10) Second fusion results of different fusion algorithms.

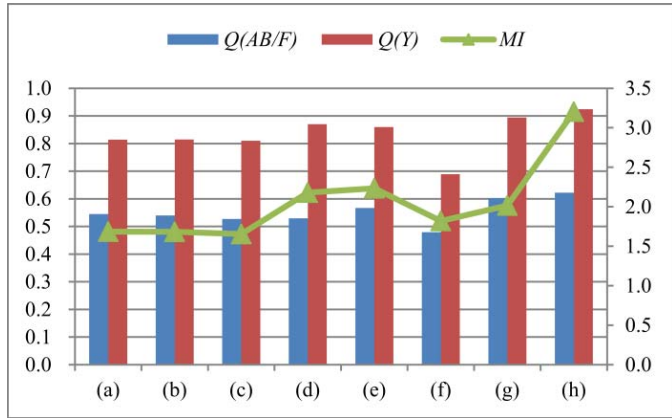


Fig. 7. Evaluation indices for fused infrared and visible images. (a) LP. (b) SIDWT. (c) NSCT. (d) NSCT-PCNN. (e) NSCT-SR. (f) CBF. (g) GFF. (h) Ours.

results in Fig. 4(i)–(o) that some of the information from the focused regions was still retained in the difference images. This indicates that the fused images obtained by these methods do not completely originate in the focused regions of the input images. Compared with those methods, the proposed algorithm transfers almost all of the useful information of

the source images to the fused images. This is because the difference images corresponding to the focused regions in Figs. 3(p) and 4(p) were close to zero. The proposed algorithm not only avoids the halo artifacts but also effectively inhibits the boundary discontinuity.

The quantitative results in Table I also demonstrate that our method is more robust and performs better than the traditional fusion methods in terms of significant extracted information and spatial consistency. The good criteria values presented here indicate that the fused image obtained by the proposed method can retain much more focused information and achieve higher similarity and correlation to the source images.

#### C. Experiments on Multimodal Medical Image Fusion

This section describes how we evaluated the performance of the proposed fusion method using five common groups of medical images consisting of different modalities [see Fig. 2(b)]. The images comprised two groups of CT and MRI images (CT/MRI), a group of T1-weighted MR images and magnetic resonance angiography (MR-T1/MRA), a group of MR-T1 and MR-T2 images (MR-T1/MR-T2), and a group comprising an MR image after Gd-DTPA and a T2-weighted image (MR-GAD/MR-T2).

TABLE III  
EVALUATION INDICES FOR SINGLE FEATURE USED IN FUSION

Source Images	Index	GFF	CS-GFF	SP-GFF	SS-GFF	CS-P	SP-P	SS-P	Ours
multifocus	$MI$	7.832	7.873	7.697	7.462	7.907	7.717	7.499	<b>8.324</b>
	$Q^{AB/F}$	0.752	0.753	0.751	0.749	0.754	0.751	0.750	<b>0.755</b>
	$Q_Y$	0.962	0.962	0.958	0.955	0.964	0.959	0.957	<b>0.968</b>
multimodal medical	$MI$	3.440	3.520	3.477	3.574	3.649	3.666	3.784	<b>4.210</b>
	$Q^{AB/F}$	0.680	0.701	0.677	0.673	0.686	0.657	0.661	<b>0.703</b>
	$Q_Y$	0.882	0.896	0.878	0.885	0.927	0.904	0.910	<b>0.946</b>
infrared-visible	$MI$	2.015	2.413	1.969	2.083	2.609	2.098	2.227	<b>3.528</b>
	$Q^{AB/F}$	0.603	<b>0.635</b>	0.592	0.598	0.607	0.567	0.575	0.626
	$Q_Y$	0.894	<b>0.924</b>	0.882	0.888	0.911	0.871	0.877	<b>0.924</b>

For the five image sets, the corresponding fusion results are given in Fig. 5. From the fused image, it is clear that LP-, SIDWT-, and NSCT-based methods suffer from the problem of contrast reduction. Moreover, it can be observed that the fused images obtained by the schemes of NSCT-PCNN and CBF have lost large amounts of image details. Compared with NSCT-SR- and GFF-based methods, it is clear that the proposed method outperformed the other fusion methods, and that its fused image has a good visual representation of both bone structure and soft tissue information. At the same time, one can see that the lesions and their vascular properties, and the soft tissue information are apparent in the fused images of the proposed scheme. Furthermore, we invited a radiologist (Prof. Xianjun Zeng, Department of the Medical Imaging, the First Affiliation Hospital of Nanchang University) to do evaluation of all the experiments. The medical expert has evaluated all the fused images by visual inspection and told us the fusion results of our method are valid and meaningful for medical analysis and diagnosis. The analysis above verifies that the proposed method was superior to other fusion methods in visual representation.

In addition to the subjective analysis, we also conducted a detailed objective analysis on the above experimental results by different fusion methods. For the five pairs of medical images, quantitative performance comparisons of our proposed method with other schemes are given in Table II. From Table II, we can observe that the  $MI$  and  $Q_Y$  values of the proposed method are always the largest, and the  $Q^{AB/F}$  of three pairs is largest and another two pairs are very close to the highest value. In other words, the proposed fusion method can more effectively extract prominent and detailed information from the various modalities of source images than other seven fusion methods.

#### D. Experiments on Infrared and Visible Image Fusion

For the last experiment, we selected five pairs of full registration source infrared-visible images [see Fig. 2(c)] to assess the performance of the proposed method. Two examples from fusion results are shown in Fig. 6 for visual comparison. From Fig. 6(a1) and (a2), it can be seen that the cars and the traffic lights are clear in the infrared image, whereas the advertising board is blurred. By contrast, cars and traffic lights almost cannot be seen in the visible image,

whereas the advertising board is clear. The results obtained from the different fusion methods are slightly different in terms of contrast and details. It is clear that the resultant image obtained with the proposed method appears natural and well preserves the brightness of the pedestrians. From Fig. 6(b1) and (b2), one can see an infrared image in which a person is standing behind the trees and close to the fence, a visible image of a scene representing a sandy path, trees, and fences. Upon observation of the results obtained from the different fusion methods, it is clear that the proposed method is superior to other methods as the person is more salient in the fused image and the landscape structure is better represented in the proposed method compared with the other methods.

Fig. 7 shows the average evaluation criteria values of the different fusion methods on five pairs of test infrared-visible images. It clearly shows that the proposed algorithm significantly outperforms the other methods for the tested images with constantly higher scores in terms of fusion metrics. These three largest criteria values confirm the objective assessment, which means the images obtained by the proposed method generally incorporate more information from the visible image together with the important targets from the infrared image.

#### E. Experiments on Single Feature Used in Fusion

Table III shows the average values of all quality indices obtained by each feature that is used to construct weight maps in our scheme (CS-P, SP-P, and SS-P) as well as the GFF scheme (CS-GFF, SP-GFF, and SS-GFF). As can be seen from the last four columns of Table III, the proposed multiple visual features-based weight construction method gives the largest metrics values compared with the method that used only one feature to construct weight maps. This indicates that the three different visual features can effectively reflect different aspects of a source image. It also demonstrates that our proposed weight construction method is more reasonable and helpful in improving fusion performance. Moreover, we can observe that CS-based fusion is superior to the SP-based and SS-based fusion when considering each feature employed in the fusion scheme. This reveals that CS has more impact on fusion weight, but it cannot obtain the most accurate expression compared with the three features because the CS,

TABLE IV  
AVERAGE RUNNING TIME OF DIFFERENT METHODS ON ALL SOURCE IMAGES

Method	Time/s
LP	0.02
SIDWT	0.08
NSCT	2.81
NSCT-PCNN	43.19
NSCT-SR	16.26
CBF	11.33
GFF	0.11
Ours	0.82

SP, and SS measures could address different aspects about visual significance of a source image and are complementary to each other.

On the other hand, when comparing each feature used in GFF scheme with our scheme, respectively, we noted that our scheme gives much better fusion performance in terms of all three metrics for multifocus image fusion, two metrics including  $MI$  and  $Q_Y$  for multimodal medical image fusion, and one metric  $MI$  for infrared-visible image fusion. It also shows that GFF scheme especially the CS-GFF method is more qualified for infrared-visible image fusion. Overall, although the performance of our scheme is not always the best, it has a very stable performance for multifocus, multimodal medical, and infrared-visible image fusion. Thus, it can be proved that the superior fusion performance can be achieved by our method.

#### F. Computational Efficiency Analysis

The computational efficiencies of different fusion methods are compared in Table IV. In our experiments, all the eight test methods are similarly implemented in MATLAB 2014a on a computer with a 3.3-GHz CPU and 8-GB RAM. The codes of the seven compared methods are available online and they are all developed based on the MATLAB. As shown in Table IV, the NSCT-PCNN method is the most time consuming one, while the NSCT-SR and CBF methods are also not efficient. This may result from the fact that the NSCT, PCNN, and SR are high computational complexity and time consuming. The GFF method uses a simple Laplace operator to construct fusion weight map, so it has a very high computational efficiency. Our method greatly improves the fusion effect while also maintaining a high computational efficiency. We believe that our method can be implemented in real-time application through a more efficient programming approach such as C++ in the near future work.

## V. CONCLUSION

In this paper, we proposed a novel multisensor image fusion method by multiple visual features measurement with gradient domain guided filtering. We present a decision map construction model for image fusion by incorporating contrast saliency, sharpness, and structural saliency as the key visual factors. The decision map construction model can effectively and

accurately measure the significance of visual features, which greatly improves the performance of the proposed method. Subsequently, the gradient domain guided filtering is used to optimize the decision map by considering the correlations between neighborhood pixels. It can more effectively inhibit halo artifacts that may produce by noisy and not aligned with object boundaries of decision map. Finally, our method with seven other popular methods is employed for the fusion of multifocus, multimodal medical, and visible-infrared images. The experimental results clearly demonstrate that the proposed algorithm can preserve the original and complementary information of multiple source images better than other fusion methods. It should be noted that the GDGIF fixed parameter setting used in this paper can generally obtain good results for all images and our method does not depend much on the exact parameter choice. Despite this, we also found that different types of source images are adapt to different parameters in our preliminary experiments. Thus, how to better choose the parameters according to different types of source images should be researched in our future work.

## REFERENCES

- [1] H. Li, X. Li, Z. Yu, and C. Mao, "Multifocus image fusion by combining with mixed-order structure tensors and multiscale neighborhood," *Inf. Sci.*, vol. 349, pp. 25–49, Jul. 2016.
- [2] J. Yuan, H. Chen, F. Sun, and Y. Huang, "Multisensor information fusion for people tracking with a mobile robot: A particle filtering approach," *IEEE Trans. Instrum. Meas.*, vol. 64, no. 9, pp. 2427–2442, Sep. 2015.
- [3] Q. Zhang and M. D. Levine, "Robust multi-focus image fusion using multi-task sparse representation and spatial context," *IEEE Trans. Image Process.*, vol. 25, no. 5, pp. 2045–2058, May 2016.
- [4] B. Yang and S. Li, "Multifocus image fusion and restoration with sparse representation," *IEEE Trans. Instrum. Meas.*, vol. 59, no. 4, pp. 884–892, Apr. 2010.
- [5] L. Wang, B. Li, and L. Tian, "Multimodal medical volumetric data fusion using 3-D discrete shearlet transform and global-to-local rule," *IEEE Trans. Biomed. Eng.*, vol. 61, no. 1, pp. 197–206, Jan. 2013.
- [6] Y. Yang, Y. Que, S. Huang, and P. Lin, "Multimodal sensor medical image fusion based on type-2 fuzzy logic in NSCT domain," *IEEE Sensors J.*, vol. 16, no. 10, pp. 3735–3745, May 2016.
- [7] C. Liu, Y. Zhang, K. Tan, and H. Yang, "Sensor fusion method for horizon detection from an aircraft in low visibility conditions," *IEEE Trans. Instrum. Meas.*, vol. 63, no. 3, pp. 620–627, Mar. 2014.
- [8] D. P. Bavirisetti and R. Dhuli, "Fusion of infrared and visible sensor images based on anisotropic diffusion and Karhunen–Loeve transform," *IEEE Sensors J.*, vol. 16, no. 1, pp. 203–209, Jan. 2016.
- [9] G. Piella, "A general framework for multiresolution image fusion: From pixels to regions," *Inf. Fusion*, vol. 4, no. 4, pp. 259–280, 2003.
- [10] P. J. Burt and E. H. Adelson, "The Laplacian pyramid as a compact image code," *IEEE Trans. Commun.*, vol. 31, no. 4, pp. 532–540, Apr. 1983.
- [11] V. S. Petrovic and C. S. Xydeas, "Gradient-based multiresolution image fusion," *IEEE Trans. Image Process.*, vol. 13, no. 2, pp. 228–237, Feb. 2004.
- [12] H. Li, B. S. Manjunath, and S. K. Mitra, "Multisensor image fusion using the wavelet transform," *Graph. Models Image Process.*, vol. 57, no. 3, pp. 235–245, 1995.
- [13] S. Ioannidou and V. Karathanassi, "Investigation of the dual-tree complex and shift-invariant discrete wavelet transforms on quickbird image fusion," *IEEE Geosci. Remote Sens. Lett.*, vol. 4, no. 1, pp. 166–170, Jan. 2007.
- [14] J. J. Lewis, R. J. O'Callaghan, S. G. Nikolov, D. R. Bull, and N. Canagarajah, "Pixel- and region-based image fusion with complex wavelets," *Inf. Fusion*, vol. 8, no. 2, pp. 119–130, 2007.
- [15] L. Guo, M. Dai, and M. Zhu, "Multifocus color image fusion based on quaternion curvelet transform," *Opt. Exp.*, vol. 20, no. 17, pp. 18846–18860, 2012.

- [16] Q.-G. Miao, C. Shi, P.-F. Xu, M. Yang, and Y.-B. Shi, "A novel algorithm of image fusion using shearlets," *Opt. Commun.*, vol. 284, no. 6, pp. 1540–1547, 2011.
- [17] S. Yang, M. Wang, L. Jiao, R. Wu, and Z. Wang, "Image fusion based on a new contourlet packet," *Inf. Fusion*, vol. 11, no. 2, pp. 78–84, 2010.
- [18] S. Li, B. Yang, and J. Hu, "Performance comparison of different multi-resolution transforms for image fusion," *Inf. Fusion*, vol. 12, pp. 74–84, Apr. 2011.
- [19] Q. Zhang and B.-L. Guo, "Multifocus image fusion using the non-subsampled contourlet transform," *Signal Process.*, vol. 89, no. 7, pp. 1334–1346, 2009.
- [20] X.-B. Qu, J.-W. Yan, H.-Z. Xiao, and Z.-Q. Zhu, "Image fusion algorithm based on spatial frequency-motivated pulse coupled neural networks in nonsubsampled contourlet transform domain," *Acta Autom. Sinica*, vol. 34, no. 12, pp. 1508–1514, 2008.
- [21] Z. Wang, Y. Ma, F. Cheng, and L. Yang, "Review of pulse-coupled neural networks," *Image Vis. Comput.*, vol. 28, no. 1, pp. 5–13, 2010.
- [22] R. Eckhorn, H. J. Reitboeck, M. Arndt, and P. Dicke, "Feature linking via synchronization among distributed assemblies: Simulations of results from cat visual cortex," *Neural Comput.*, vol. 2, no. 3, pp. 293–307, 1990.
- [23] Y. Liu, S. Liu, and Z. Wang, "Multi-focus image fusion with dense SIFT," *Inf. Fusion*, vol. 23, pp. 139–155, May 2015.
- [24] S. Das and M. K. Kundu, "A neuro-fuzzy approach for medical image fusion," *IEEE Trans. Biomed. Eng.*, vol. 60, no. 12, pp. 3347–3353, Dec. 2013.
- [25] V. Harikumar, P. P. Gajjar, M. V. Joshi, and M. S. Raval, "Multiresolution image fusion: Use of compressive sensing and graph cuts," *IEEE J. Sel. Topics Appl. Earth Observ. Remote Sens.*, vol. 7, no. 5, pp. 1771–1780, May 2014.
- [26] H. Liu, S. Li, and L. Fang, "Robust object tracking based on principal component analysis and local sparse representation," *IEEE Trans. Instrum. Meas.*, vol. 64, no. 11, pp. 2863–2875, Nov. 2015.
- [27] Z. Liu, H. Yin, Y. Chai, and S. X. Yang, "A novel approach for multimodal medical image fusion," *Exp. Syst. Appl.*, vol. 41, no. 16, pp. 7425–7435, 2014.
- [28] S. Li, H. Yin, and L. Fang, "Remote sensing image fusion via sparse representations over learned dictionaries," *IEEE Trans. Geosci. Remote Sens.*, vol. 51, no. 9, pp. 4779–4789, Sep. 2013.
- [29] Y. Liu, S. Liu, and Z. Wang, "A general framework for image fusion based on multi-scale transform and sparse representation," *Inf. Fusion*, vol. 24, pp. 147–164, Jul. 2015.
- [30] S. Li and B. Yang, "Multifocus image fusion using region segmentation and spatial frequency," *Image Vis. Comput.*, vol. 26, no. 7, pp. 971–979, 2008.
- [31] J. Liang, Y. He, D. Liu, and X. Zeng, "Image fusion using higher order singular value decomposition," *IEEE Trans. Image Process.*, vol. 21, no. 5, pp. 2898–2909, May 2012.
- [32] H. Zhao, Z. Shang, Y. Y. Tang, and B. Fang, "Multi-focus image fusion based on the neighbor distance," *Pattern Recognit.*, vol. 46, pp. 1002–1011, Mar. 2013.
- [33] M. Nejati, S. Samavi, and S. Shirani, "Multi-focus image fusion using dictionary-based sparse representation," *Inf. Fusion*, vol. 25, pp. 72–84, Sep. 2015.
- [34] B. K. S. Kumar, "Image fusion based on pixel significance using cross bilateral filter," *Signal, Image Video Process.*, vol. 9, no. 5, pp. 1193–1204, 2015.
- [35] R. Shen, I. Cheng, J. Shi, and A. Basu, "Generalized random walks for fusion of multi-exposure images," *IEEE Trans. Image Process.*, vol. 20, no. 12, pp. 3634–3646, Dec. 2011.
- [36] J. Sun, H. Zhu, Z. Xu, and C. Han, "Poisson image fusion based on Markov random field fusion model," *Inf. Fusion*, vol. 14, no. 3, pp. 241–254, 2013.
- [37] S. Li, X. Kang, and J. Hu, "Image fusion with guided filtering," *IEEE Trans. Image Process.*, vol. 22, no. 7, pp. 2864–2875, Jul. 2013.
- [38] K. He, J. Sun, and X. Tang, "Guided image filtering," *IEEE Trans. Pattern Anal. Mach. Intell.*, vol. 35, no. 6, pp. 1397–1409, Jun. 2013.
- [39] Z. Li, J. Zheng, Z. Zhu, W. Yao, and S. Wu, "Weighted guided image filtering," *IEEE Trans. Image Process.*, vol. 24, no. 1, pp. 120–129, Jan. 2015.
- [40] F. Kou, W. Chen, C. Wen, and Z. Li, "Gradient domain guided image filtering," *IEEE Trans. Image Process.*, vol. 24, no. 11, pp. 4528–4539, Nov. 2015.
- [41] R. Hassen, Z. Wang, and M. M. A. Salama, "Objective quality assessment for multiexposure multifocus image fusion," *IEEE Trans. Image Process.*, vol. 24, no. 9, pp. 2712–2724, Sep. 2015.
- [42] Z. Wang, A. C. Bovik, H. R. Sheikh, and E. P. Simoncelli, "Image quality assessment: From error visibility to structural similarity," *IEEE Trans. Image Process.*, vol. 13, no. 4, pp. 600–612, Apr. 2004.
- [43] W. Huang and Z. Jing, "Evaluation of focus measures in multi-focus image fusion," *Pattern Recognit. Lett.*, vol. 28, no. 4, pp. 493–500, 2007.
- [44] S. K. Nayar and Y. Nakagawa, "Shape from focus," *IEEE Trans. Pattern Anal. Mach. Intell.*, vol. 16, no. 8, pp. 824–831, Aug. 1994.
- [45] Z. Zhou, S. Li, and B. Wang, "Multi-scale weighted gradient-based fusion for multi-focus images," *Inf. Fusion*, vol. 20, no. 1, pp. 60–72, 2014.
- [46] B. Zitová and J. Flusser, "Image registration methods: A survey," *Image Vis. Comput.*, vol. 21, pp. 977–1000, Oct. 2003.
- [47] G. Qu, D. Zhang, and P. Yan, "Information measure for performance of image fusion," *Electron. Lett.*, vol. 38, no. 7, pp. 313–315, Mar. 2002.
- [48] C. S. Xydeas and V. Petrović, "Objective image fusion performance measure," *Electron. Lett.*, vol. 36, no. 4, pp. 308–309, 2000.
- [49] C. Yang, J.-Q. Zhang, X. Wang, and X. Liu, "A novel similarity based quality metric for image fusion," *Inf. Fusion*, vol. 9, no. 2, pp. 156–160, 2008.



Dr. Yang received the title of Jiangxi Province Young Scientist in 2012.

**Yong Yang** (M'13–SM'16) received the Ph.D. degree in biomedical engineering from Xi'an Jiaotong University, Xi'an, China, in 2005.

From 2009 to 2010, he was a Post-Doctoral Research Fellow with Chonbuk National University, Jeonju, South Korea. He is currently a Full Professor with the School of Information Technology, Jiangxi University of Finance and Economics, Nanchang, China. His current research interests include image fusion and segmentation, medical image processing and analysis, and pattern recognition.



**Yue Que** received the B.S. degree in educational technology from Nanchang Hangkong University, Nanchang, China, in 2013. He is currently pursuing the M.S. degree in computer technology with the Jiangxi University of Finance and Economics, Nanchang.

His current research interests include image fusion, fuzzy pattern recognition, and image processing.



**Shuying Huang** (M'14) received the Ph.D. degree in computer application technology from the Ocean University of China, Qingdao, China, in 2013.

She is currently an Associate Professor with the School of Software and Communication Engineering, Jiangxi University of Finance and Economics, Nanchang, China. Her current research interests include image and signal processing, and pattern recognition.



**Pan Lin** (M'16) received the Ph.D. degree in biomedical engineering from Xi'an Jiaotong University, Xi'an, China, in 2005.

From 2007 to 2011, he was a Post-Doctoral Researcher with the Center for Mind/Brain Sciences, University of Trento, Trento, Italy. From 2013 to 2014, he was a Research Fellow with the Mclean Hospital, Harvard Medical School, Boston, MA, USA. Since 2011, he has been an Associate Professor with the Institute of Biomedical Engineering, Xi'an Jiaotong University. His current research interests include multimodal MRI imaging, medical image processing, image processing, and pattern recognition.